MRI-assisted dual motion correction for myocardial perfusion defect detection in PET imaging

Xinhui Wang
Department of Electrical and Computer Engineering, Oakland University, Rochester, MI 48309, USA

Arman Rahmim
Department of Radiology, Johns Hopkins University, Baltimore, MD 21287, USA

Jing Tang[a)]
Department of Electrical and Computer Engineering, Oakland University, Rochester, MI 48309, USA

(Received 27 January 2017; revised 11 June 2017; accepted for publication 12 June 2017; published 9 August 2017)

Purpose: Myocardial perfusion (MP) PET imaging is a powerful tool in risk assessment and stratification of patients with coronary artery disease. Involuntary organ motion degrades cardiac PET image resolution, while respiratory and/or cardiac gating to freeze the motion leads to noisier reconstructed images due to reduced counts in the gated frames. In this work, we propose an MRI-assisted dual motion correction method to compensate for respiratory and cardiac motion in MP PET data and study the impact of dual motion correction on MP defect detection using systematically designed experiments.

Methods: The proposed dual motion correction method addresses the respiratory motion before correcting the cardiac motion among the respiratory motion corrected cardiac gates. The respiratory motion is estimated from the respiratory-gated only PET images and compensated within a 4D motion-incorporated image reconstruction algorithm. The cardiac motion is then corrected using the motion vector fields estimated from the corresponding cardiac-gated MR images. To evaluate the proposed method, we performed experiments using the standard XCAT phantom and two individual-specific volunteer XCAT phantoms. For each of the three phantoms, we simulated four dual-gated Rb-82 MP PET imaging datasets, one with normal perfusion and the other three with 50% nontransmural, 75% nontransmural, and transmural regionally reduced perfusion. The corresponding cardiac-gated MR images were simulated by the SIMRI simulator, with the sequence specified to be 3D T1-weighted as used in a protocol of a clinical PET/MRI scanner. We quantitatively evaluated the reconstructed images with no motion correction, only respiratory motion correction and dual motion correction, in terms of the myocardium to blood pool contrast and the trade-off between the noise and the normal to defect contrast. Using the channelized Hotelling observer, we performed receiver operating characteristic analysis for the task of detecting perfusion abnormalities with various myocardial coverages.

Results: Compared with no motion correction, the respiratory motion correction was demonstrated to improve the myocardium to blood pool contrast as well as the trade-off between the noise and the normal to defect contrast, on top of which the cardiac motion correction furthered the improvement. In the task of detecting regional perfusion defects, transmural or different levels of nontransmural, the respiratory motion correction significantly increased the defect detectability compared with no motion correction. Additionally, the respiratory and cardiac motion correction significantly improved the defect detection compared with the respiratory motion correction alone. Furthermore, the separability of the transmural and nontransmural defects was also improved by the proposed MRI assisted dual motion correction method.

Conclusions: The proposed dual respiratory and cardiac motion correction technique improves the accuracy of PET quantification and MP defect detection and classification, which shows its promise for clinical applications especially in cardiac PET/MR imaging. [https://doi.org/10.1002/mp.12429]

Key words: cardiac motion, motion correction, myocardial perfusion defect detection, PET/MRI, respiratory motion

1. INTRODUCTION

Myocardial perfusion (MP) PET imaging plays an important role in clinical diagnosis and demonstrates its prognostic value in risk stratification for patients with coronary artery disease.[1–4] Detection and assessment of myocardial ischemia is clinically important as the extent of an infarct is a good indicator of whether revascularization of stenotic coronary

lesions would improve a patient's functional status and outcome.[5,6] Transmural infarcts are associated with a higher likelihood of adverse cardiac events, poorer prognosis, and lack of recovery. The identification of nontransmural infarction implies that viable myocardium is present and the patient would benefit from revascularization procedures.[7,8]

Cardiac PET image resolution is degraded by involuntary cardiac and respiratory motion. Heart beating introduces notable visual and quantitative degradation in cardiac PET images. The base of the heart typically moves $\sim$13 mm along the long axis toward the apex[9], while the myocardial walls thicken from $\sim$10 mm to greater than 15 mm between the end diastole and the end systole.[10,11] Coronary arteries have been shown to move 8–23 mm during the cardiac cycle.[12] As the cardiac imaging protocols take longer than minutes, the data are inevitably averaged over many respiratory cycles if images are reconstructed without respiratory motion compensation. Translational displacement of the heart caused by respiration is most in the craniocaudal direction. The magnitude is comparable with the myocardial wall thickness averaging $\sim$12 mm with the maximum exceeding 20 mm.[13,14] With an intrinsic PET system resolution of 5 mm full width half maximum (FWHM), the effective resolution becomes 15 mm FWHM considering the respiratory motion of 12 mm amplitude.[14]

To reduce motion artifacts, cardiac gating, respiratory gating, and dual gating techniques have been developed in MP PET imaging.[15–19] Other than alleviating motion blur, cardiac-gated imaging allows simultaneous assessment of left ventricle contractile function thus providing direct information on the therapeutic efficacy of the metabolic intervention.[20,21] Despite the benefits brought by gating, it is unavoidable that individual-gated frames contain reduced counts which lead to noisier reconstructed images. Technique development to estimate and compensate for cardiac and respiratory motion has become a research focus of PET imaging in the last decade.[22,23] Two general schemes of motion correction have been considered; one is to register and sum independently reconstructed image frames[24,25] and the other is to incorporate the motion within the image reconstruction procedure.[26–29] Theoretic comparisons have been made between post-reconstruction and within-reconstruction motion compensation techniques and less or comparable variance has been shown in the latter.[30,31] Simulation studies have also shown that motion compensation during reconstruction reaches better quantitative accuracy than after-reconstruction motion correction.[32]

Cardiac, respiratory, and dual gating/motion correction studies have shown the creation of "motion free" cardiac PET (and SPECT) images with reduced blurring effects and improved quality, evaluated by various mathematical metrics and/or in terms of perfusion defect detection. Performing dual respiratory-cardiac gating, Chan et al. demonstrated increased myocardium to blood pool contrast and myocardium to defect contrast at the expenses of increased noise in stationary cardiac SPECT imaging.[33] Petibon et al. proposed to use cardiac motion estimated from tagged-MR images for correction and demonstrated improved defect versus myocardium contrast recovery and lesion detectability in cardiac PET images.[34] Lamare et al. compared different approaches in combining dual-gated cardiac PET acquisition and arrived at higher signal to noise ratio, higher contrast and coefficient of variation in the motion-corrected cardiac images compared with images with no motion correction.[35] Up until this point, we are not aware of a study to correct dual motion in cardiac PET imaging for the purpose of MP defect detection.

Appreciating the knowledge gained from previous studies, we propose a new two-step dual respiratory and cardiac motion correction scheme for detecting MP defects. The first step involves estimating nonrigid respiratory motion and incorporating the respiratory motion in a four-dimensional (4D) motion-corrected image reconstruction method. This step results in respiratory motion-corrected cardiac gates, among which the cardiac motion will be estimated and corrected in the second step. Given the challenge of estimating cardiac wall motion from gated PET images with poor intrinsic resolution, we estimate the motion for heart beat compensation from corresponding cardiac-gated MR images. This is reasoned by the availability of simultaneous PET/MRI scanners for cardiac imaging[36] and the demonstrated feasibility and advantage of using the MR-derived motion fields for nonrigid motion correction for PET images.[37] To evaluate the effectiveness of this dual motion correction scheme, we study the detection of MP abnormalities of different coverages from normal perfusion myocardium and the classification of transmural and nontransmural defects. More specifically, this work answers the question on whether respiratory motion correction affects MP defect detection and whether cardiac motion correction on top of it contributes to this task as well.

2. METHODS

In this section, we describe the respiratory/cardiac motion estimation and correction techniques we developed. For respiratory motion compensation, we use motion-incorporated 4D image reconstruction with the motion estimated from respiratory-gated only PET images. For cardiac motion correction, we estimate the motion vector fields (MVFs) from cardiac-gated MR images and apply the correction to the respiratory motion-corrected cardiac-gated PET images. A diagram depicting the overall approach is shown in Fig. 1. The detail description of the techniques follows.

2.A. Respiratory motion

We developed a 4D motion-incorporated image reconstruction technique to use the data collectively and correct respiratory motion in the maximum-likelihood (ML) expectation-maximization (EM) reconstruction process.[38] The effect of respiratory motion within each cardiac-gated MP images is to be corrected, preparing for the cardiac motion correction at the next stage. To avoid the excessive noise in the dual-gated images, we reconstruct the respiratory-gated only (no cardiac gating) images from which we estimate the respiratory

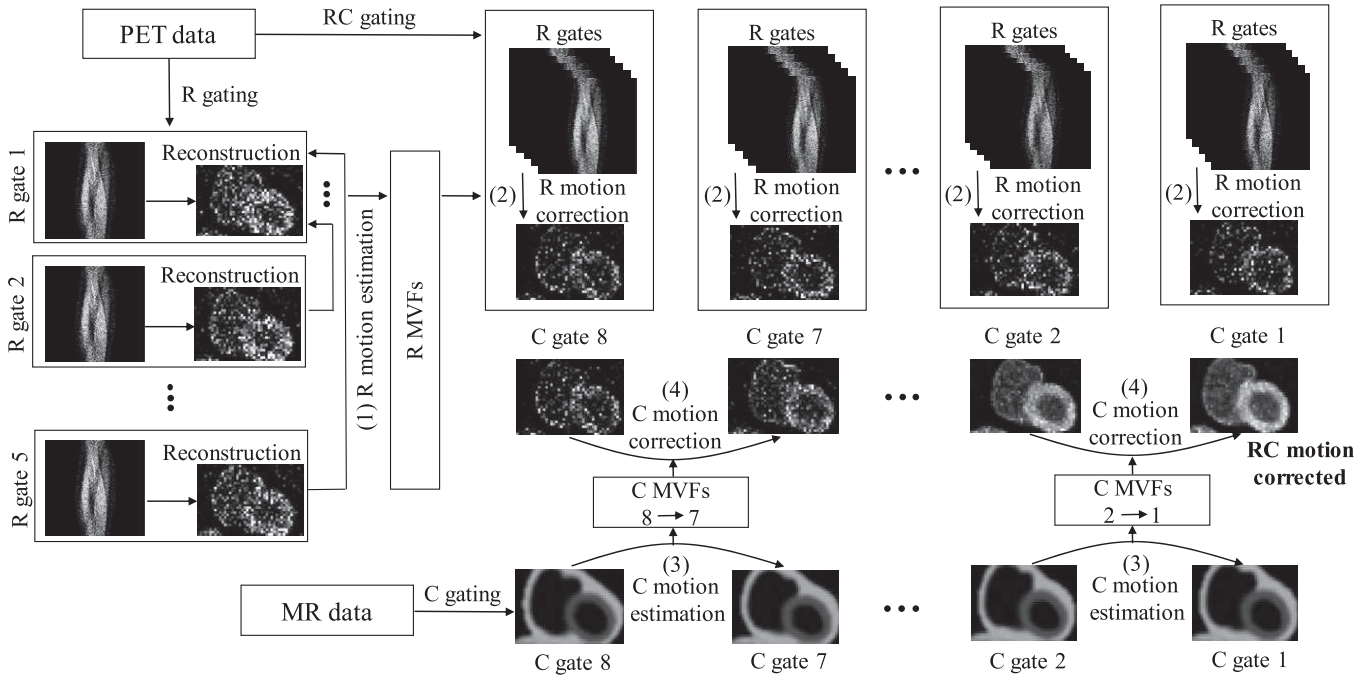

FIG. 1. Diagram for the proposed MRI assisted dual PET respiratory (R) and cardiac (C) motion correction approach. (1) The respiratory MVFs are estimated from the respiratory-gated only (no cardiac gating) PET images; (2) Within each cardiac gate, the respiratory motion is corrected by the 4D motion-incorporated image reconstruction technique; (3) The cardiac MVFs are estimated from the cardiac-gated MR images; (4) The cardiac motion is corrected among the respiratory motion-corrected cardiac gates to reach at a dual motion-corrected image.

motion from each gate n to the reference gate 1 at the end-expiration.[39] Note that we treat the heart beat as a local movement with regard to the respiratory motion. A nonrigid image registration method with B-spline transform[40] is used to estimate MVFs from each gate to the reference gate. The mean square difference (MSD) is used as the cost function of the registration algorithm. The MSD is defined as

$$\mathrm{MSD}(\mathbf{m}) = \sum_{\mathbf{r}} [f_1(\mathbf{r}) - f_n(\mathbf{r} + \mathbf{m}(\mathbf{r}))]^2, \tag{1}$$

where $\mathbf{r} = [x, y, z]^T$ is a 3D spatial coordinate, and $\mathbf{m}$ is the 3D MVF that supposedly warps the reference gate image $f_1(\mathbf{r})$ to the target gate image $f_n(\mathbf{r})$. The nonrigid B-spline image registration is implemented with the Insight Segmentation and Registration Toolkit open source software.[41] Within each cardiac gate, the respiratory-gated data are reconstructed collectively to a respiratory motion-suppressed image at the reference phase. The iterative procedure for the 4D motion-corrected EM reconstruction algorithm is given by

$$\mathbf{f}_1^{k+1} = \frac{\mathbf{f}_1^k}{\sum_{n=1}^N \mathbf{M}_{1\to n}^{\mathrm{T}} \mathbf{C}^{\mathrm{T}} \mathbf{1}} \sum_{n=1}^N \mathbf{M}_{1\to n}^{\mathrm{T}} \mathbf{C}^{\mathrm{T}} \frac{\mathbf{g}_n}{\mathbf{C}\mathbf{M}_{1\to n}\mathbf{f}_1^k}, \tag{2}$$

where $\mathbf{f}_1^k$ is the reference frame image estimate of the kth iteration, $\mathbf{g}_n$ is the respiratory-gated data with $n = 1,\ldots,N$, N is the number of gates, $\mathbf{M}_{1\to n}$ denotes the estimated respiratory motion operator that maps the reference respiratory gate 1 to the target respiratory gate n, $\mathbf{C}$ is the system matrix, $\mathbf{1}$ is a column vector with all elements equal to 1, and T represents the transpose.

2.B. Cardiac motion

The cardiac motion correction among the respiratory motion-corrected cardiac gates is performed with the MVFs estimated from adjacent cardiac-gated MR images. The motion estimation between two cardiac gates is treated as a constrained minimization problem.[42] The estimation problem is solved by finding the 3D MVF $\mathbf{m}$ that minimizes the cost function

$$E_I(\mathbf{m}) + \alpha E_s(\mathbf{m}), \tag{3}$$

where $E_I(\mathbf{m})$ is the image-matching error term and $E_s(\mathbf{m})$ is a regularization term with α as the weight. The image-matching error is defined as the intensity difference between the normalized first frame and the warped correspondence of the normalized second frame with a given MVF

$$E_I(\mathbf{m}) \triangleq \sum_{\mathbf{r}} [f_1(\mathbf{r}) - f_2(\mathbf{r} + \mathbf{m}(\mathbf{r}))]^2, \tag{4}$$

where $\mathbf{r}$ is the 3D spatial coordinate of a voxel, f_1 and f_2 are the two adjacent cardiac gates from which an MVF is to be estimated, and $\mathbf{m}$ is the MVF that supposedly warps f_2 to f_1. The strain energy function for a linear isotropic elastic material[43] is chosen to serve as the regularizing constraint

$$E_S(\mathbf{m}) \triangleq \frac{1}{2}\sum_{\mathbf{r}} \lambda(u_x + v_y + w_z)^2 + \sum_{\mathbf{r}} \mu(u_x^2 + v_y^2 + w_z^2) + \frac{1}{2}\sum_{\mathbf{r}} \mu[(u_y + v_x)^2 + (u_z + w_x)^2 + (v_z + w_y)^2], \tag{5}$$

where u, v, and w are the component of $\mathbf{m}$ in the x, y, and z directions of the Cartesian coordinate, and u_x is the notation for partial derivative $\partial u/\partial x$. The parameters λ and μ are the 1st and 2nd Lamé constants which are determined from experimental data and a finite element model for the left ventricle.[44] The MVF is estimated using an iterative method to minimize a convex approximation of the cost function, which includes the first-order Taylor expansion of $E_I(\mathbf{m})$.[42]

With the estimated gate-to-gate cardiac MVFs, we correct the cardiac motion between adjacent respiratory motion-corrected cardiac gates. The end-diastolic frame (cardiac gate 1) serves as the reference gate and the motion-corrected summation starts from the last gate (gate 8). To be more specific, the MVF estimated from the 7th and the 8th frames is used to warp the 8th frame and added to the 7th frame. Then the motion-corrected summation of the 8th and the 7th gates is warped by the MVF estimated from the 6th and the 7th frames and added to the 6th frame, and so on.

3. EXPERIMENTS AND EVALUATION

To study the effect of respiratory and cardiac motion correction on perfusion defect detection, we simulated dual-gated MP PET imaging data and the corresponding cardiac-gated MR images. The standard XCAT phantom[45] and the individual-specific XCAT phantoms[46] were used to generate the dual-gated MP PET data with normal and regionally reduced perfusion. We first evaluated the images reconstructed with and without respiratory/cardiac motion correction using mathematical image quality metrics. Using the channelized Hotelling observer (CHO), we then performed task-based evaluation for MP defect detection.

3.A. Data simulation

3.A.1. Dual-gated cardiac PET data simulation

Using the standard XCAT phantom,[45] we simulated four MP 5D imaging datasets, one with normal perfusion and the other three with 50% nontransmural, 75% nontransmural, and transmural regionally reduced perfusion. The activities of the organs including the blood pool and the myocardium were simulated based on the time activity curves (TACs) measured from the Rb-82 PET images of five patients with normal cardiac function. The TACs of the patients were smoothed and averaged to acquire a set of TACs representing the typical Rb-82 biodistribution for simulation.[47] The transmural perfusion defect spanned 40° over the anterior-lateral region and 1.5 cm over the long-axis direction. Its activity was 10% less than the normal activity. The nontransmural perfusion defects had the same coverages and activity as the transmural defect other than being on the endocardium spanning 50% or 75% of the myocardium wall. Analytical simulations were performed to create dual-gated PET data with five respiratory and eight cardiac gates. Attenuation and normalization effects were modeled in the simulations (and were also corrected in all the reconstruction methods). The noise-free sinograms were scaled corresponding to cumulated activity of the clinical count level with prescan delay time of 30 s. For each of the four cases with the normal, 50% nontransmural defect, 75% nontransmural defect, and transmural defect cases, 200 noise realizations were generated.

Similar to the data simulation of the standard XCAT phantom, we also simulated imaging datasets of normal perfusion and three perfusion defect coverages using two individual-specific XCAT phantoms developed based on MRI acquisitions of volunteers.[46] In the customized phantoms, the body and organ sizes/shapes of the volunteers all vary from those in the standard XCAT phantom. Furthermore, the nonrigid respiratory motion trends were derived from dynamic MRI acquisitions of the individual volunteers. As a result, they are also different from the general trend defined in the standard XCAT phantom. The volunteers A and B were selected from the studies 2 and 3 of the available five customized phantoms. The former has relatively large and the latter has relatively small respiratory motion amplitudes among all the phantoms. The corresponding defects on these phantoms were defined similarly to those on the standard XCAT phantom.

3.A.2. Cardiac-gated MR data simulation

For each of the three (the standard and the two customized) phantoms simulated, the corresponding MR image simulations were performed using the open source simulator SIMRI,[48] which we modified to input the T1, T2, and proton density maps created using the corresponding XCAT phantoms with known tissue values. The SIMRI takes into account the main static field value and enables realistic simulations of the chemical shift artifact including off-resonance phenomena. To simulate a protocol used in a clinical PET/MRI scanner, we specified the sequence to be 3D T1-weighted (turbo spin echo, echo time/repetition time = 2.3 ms/4 ms) with low flip angle of 2°.[49] We simulated the eight cardiac gates at the end expiratory gate, as it was used as the reference gate for respiratory motion correction.

3.B. Evaluation

3.B.1. Mathematical image quality metrics

To evaluate the reconstructed images with and without respiratory or cardiac motion correction, we first calculated the myocardium to blood pool contrast from images with normal myocardial activity. From n noise realizations, the contrast is defined as

$$\mathrm{C_{MP}} = \frac{1}{n}\sum_{j=1}^{n}\frac{\bar{f}_{\mathrm{M}}^{j} - \bar{f}_{\mathrm{P}}^{j}}{\bar{f}_{\mathrm{M}}^{j} + \bar{f}_{\mathrm{P}}^{j}}, \tag{6}$$

where $\bar{f}_{\mathrm{M}}^{j}$ and $\bar{f}_{\mathrm{P}}^{j}$ are the mean activity concentration values from the myocardium (M) and blood pool (P) regions of the jth noise realization, respectively. The myocardium and blood pool regions are defined in four consecutive slices of the short axis motion-free image (the reference respiratory and

cardiac gate) with smaller volumes to reduce partial volume effects.

For the purpose of defect detection, we evaluated the noise versus contrast recovery on the region of interest (ROI) where the defect resides. The normalized standard deviation (NSD) and the contrast between the normal and abnormal activities (for transmural and nontransmural defects) were calculated for the images reconstructed with and without respiratory and/or cardiac motion correction. The ensemble NSD was calculated from the reconstructed images with normal perfusion activity

$$\mathrm{NSD} = \frac{1}{m}\sum_{i=1}^{m}\frac{\sqrt{\frac{1}{n-1}\sum_{j=1}^{n}\left(f_i^j - \bar{f}_i\right)^2}}{\bar{f}_i}, \tag{7}$$

where f_i^j denotes the ith reconstructed voxel intensity from the jth noise realization, $\bar{f}_i = \frac{1}{n}\sum_{j=1}^{n} f_i^j$ is the ensemble mean value of voxel i, and m is the number of voxels in the ROI and n is the number of noise realizations. The contrast was defined as

$$\mathrm{C_{ND}} = \frac{1}{n}\sum_{j=1}^{n}\frac{\bar{f}_{\mathrm{N}}^j - \bar{f}_{\mathrm{D}}^j}{\bar{f}_{\mathrm{N}}^j + \bar{f}_{\mathrm{D}}^j}, \tag{8}$$

where $\bar{f}_{\mathrm{N}}^j$ and $\bar{f}_{\mathrm{D}}^j$ are the mean activity values from the normal (N) and the defect (D) ROI regions of the jth noise realization, respectively. The contrast recovery ratio was defined as the ratio between the estimated contrast from the reconstructed images and the true contrast when there was no respiratory or cardiac motion.

3.B.2. Defect detectability

We performed receiver operating characteristic (ROC) analysis to evaluate the effect of respiratory and cardiac motion correction in the MP defect detection task. We used a CHO with four octave-wide rotationally symmetric frequency channels to generate ratings for the defect-absent and defect-present images.[50] Each of the reconstructed images was reoriented and the short-axis slice covering the centroid voxel of the perfusion defect region was centered and cropped to the channel template size. The CHO resulting ratings were used to estimate the ROC curves with the LABROC4 program.[51] This program estimates the area-under-curve (AUC) value of an ROC curve and its standard deviation. To compare two ROC estimates and determine if there was a statistically significant difference between them, we used the CLABROC program.[52]

4. RESULTS

Before displaying the reconstructed PET images and analyzing the results, we first show the simulated cardiac-gated MR images from which the cardiac MVFs were estimated as described in the Methods section. Figure 2 shows the center transaxial slices of the simulated MR images corresponding to the standard XCAT phantom and the two customized XCAT phantoms at the end-diastolic and the end-systolic (of the eight) frames. One can appreciate the good contrast among different tissue types and also notice the relatively uniform left ventricular myocardium.

To demonstrate the effect of respiratory and cardiac motion correction, we present the reconstructed PET images with no motion correction, with respiratory (R) motion correction, and with both respiratory and cardiac (RC) motion correction. Figure 3 shows the images reconstructed from simulation of the standard XCAT and the two individual-specific phantoms. The images were rotated to show the central

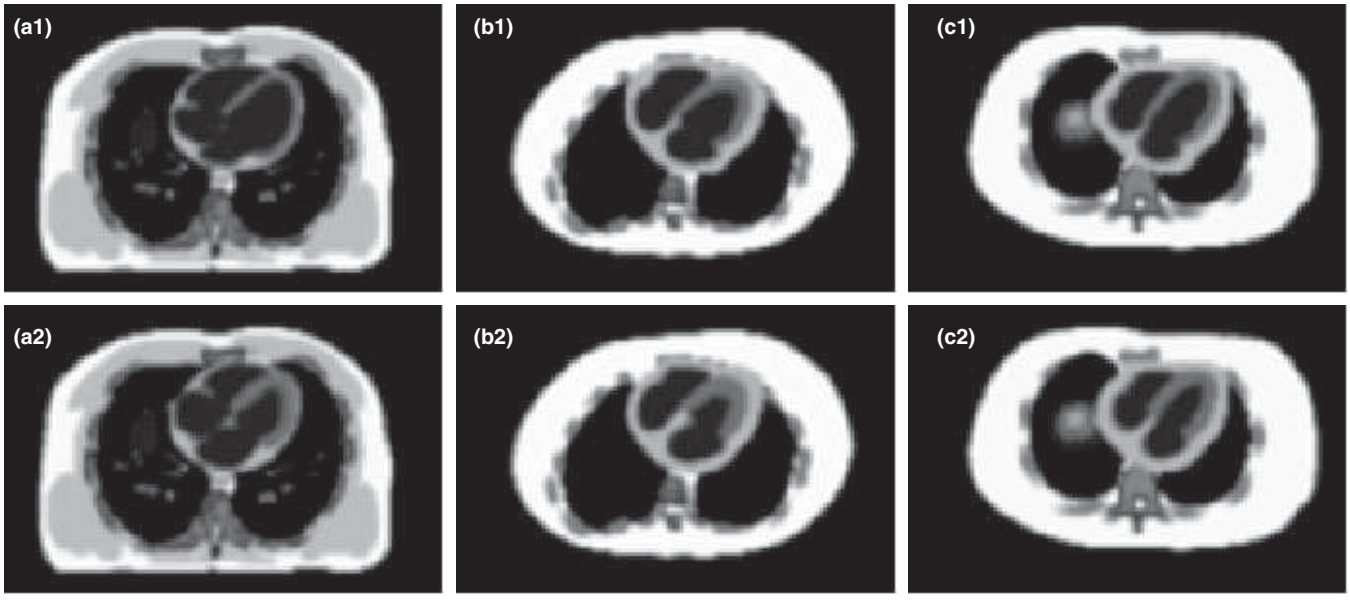

FIG. 2. Transaxial slices of the simulated cardiac-gated MR images, (a) the standard XCAT phantom, (b) the volunteer A-customized phantom, and (c) the volunteer B-customized phantom at (1) the end-diastolic and (2) the end-systolic (of the eight gated) frames, from which the cardiac MVFs were estimated for the PET image motion correction.

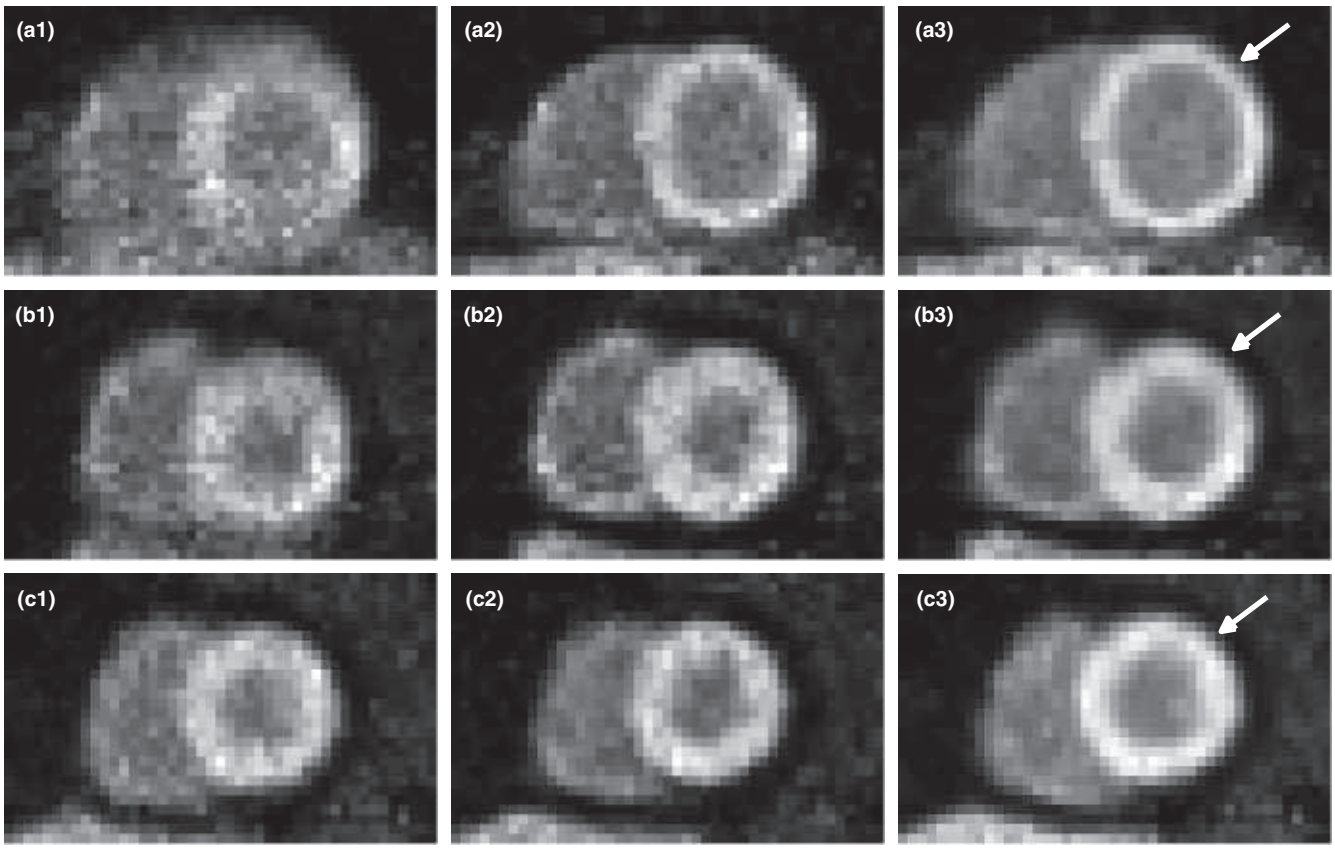

FIG. 3. Short-axis view of the images reconstructed with (left to right) (1) no motion correction, (2) R motion correction, and (3) RC motion correction; (top to bottom) (a) from the standard XCAT phantom, (b) from the volunteer A-customized phantom, and (c) from the volunteer B-customized phantom. One noise realization of each case with a transmural defect, the arrows pointing to the defects.

slice of the left ventricle in the short-axis view. Images of one noise realization (out of the 200) with the transmural defect are plotted. The R motion correction reduces the blur in the vertical direction of the images (column 1 compared with column 2 in Fig. 3) and the C motion correction on top of it enlarges the blood pool (end-diastole serving as the reference cardiac gate), i.e., the motion artifact due to the myocardial contraction is minimized (column 2 compared with column 3 in Fig. 3).

We first performed quantitative evaluation of the reconstructed images by comparing the myocardium to blood pool contrasts. The contrasts measured from the standard XCAT phantom images reconstructed using different reconstruction methods are plotted against the iteration number in Fig. 4(a). As shown in the plot, the myocardium to blood pool contrast was improved from 0.19 to 0.25 (at the 2nd iteration) when the respiratory motion correction was incorporated compared with no motion correction. The contrast was further increased from 0.25 to 0.35 (at the 2nd iteration) after performing the cardiac motion correction on top of the respiratory motion correction, compared with the respiratory motion correction alone. The myocardium and blood pool contrasts measured from the volunteer A and B phantom images are plotted against the iteration number in Figs. 4(b) and 4(c). The effect of respiratory and cardiac motion correction on the myocardium and blood pool contrast is shown similarly in the two customized XCAT phantoms. Respiratory motion correction improved the contrast in the volunteer A from 0.22 to 0.25 and in the volunteer B from 0.22 to 0.28 (at the 2nd iteration) compared with no motion correction. On top of the respiratory motion correction, the added cardiac motion correction further increased the contrast in the volunteer A from 0.25 to 0.35 and in the volunteer B from 0.28 to 0.37 (at the 2nd iteration).

Figure 5(a) presents the variation of the noise versus contrast recovery ratio for the standard XCAT phantom with each of the three (the two nontransmural, 50% and 75%, and the transmural) perfusion defects, respectively. In all the three cases, the respiratory motion correction significantly increases the contrast between the normal and the defect perfusion on the ROI at a comparable noise level. The contrast recovery for the 50% nontransmural defect increases from 23% to 57%, while the increase of the contrast recovery for the 75% nontransmural defect is from 29% to 61% and for the transmural defect from 41% to 68% [at the 2nd iteration in Fig. 5(a)]. Compared with the respiratory motion correction only result, the added cardiac motion correction noticeably reduces the noise while further improving the recovered contrast to over 90% in all the three defect cases [Fig. 5(a)]. The noise versus contrast recovery ratio curves calculated from simulation of the volunteer A and B phantoms are plotted in Figs. 5(b) and 5(c). The effect of

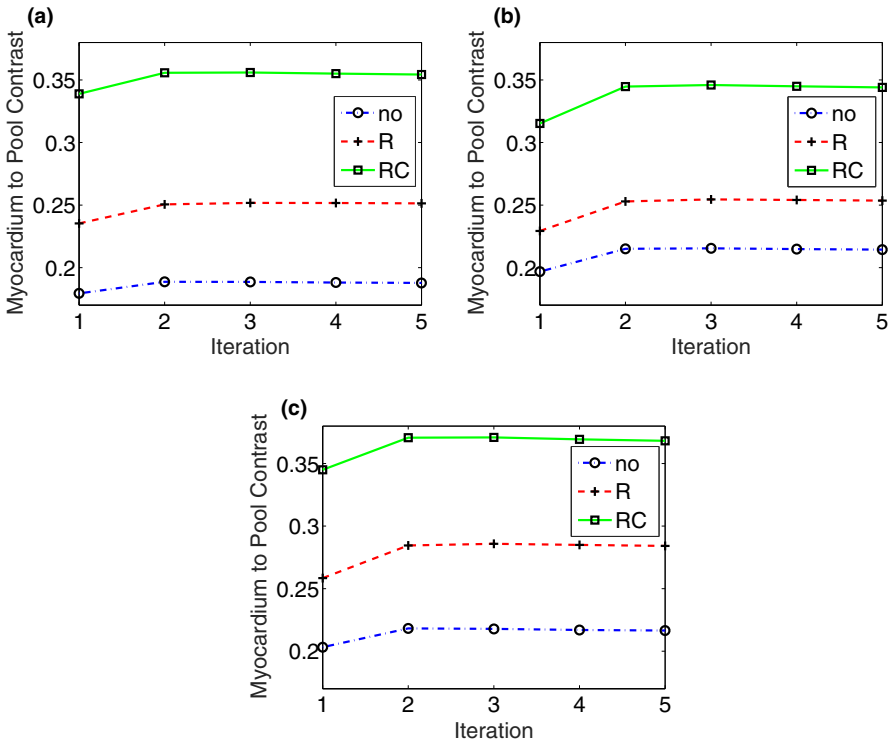

FIG. 4. Contrast between the myocardium and the blood pool varying along with the iteration number (of image reconstruction) from (a) the standard XCAT phantom, (b) the volunteer A-customized XCAT phantom, and (c) the volunteer B-customized XCAT phantom images reconstructed with the no motion correction (no), R motion-corrected (R), and RC motion-corrected (RC) methods. [Color figure can be viewed at wileyonlinelibrary.com]

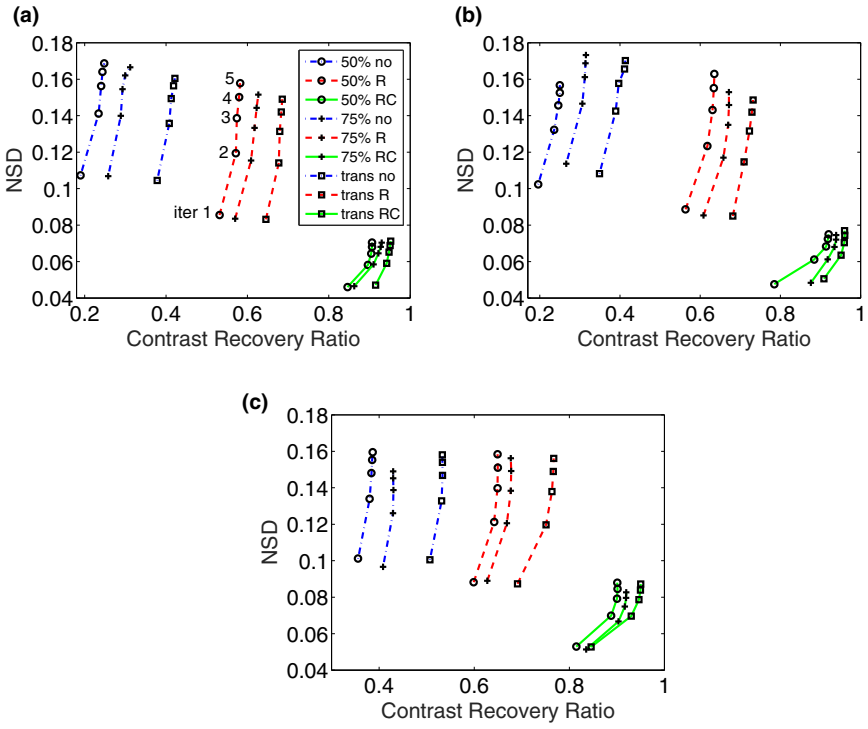

FIG. 5. NSD versus contrast recovery ratio along with the iteration number (of image reconstruction) plots from (a) the standard XCAT phantom, (b) the volunteer A-customized phantom, and (c) the volunteer B-customized phantom in the 50% nontransmural, the 75% nontransmural, and the transmural defect ROI from the images reconstructed with the no motion correction (no), R motion-corrected (R), and RC motion-corrected (RC) methods. [Color figure can be viewed at wileyonlinelibrary.com]

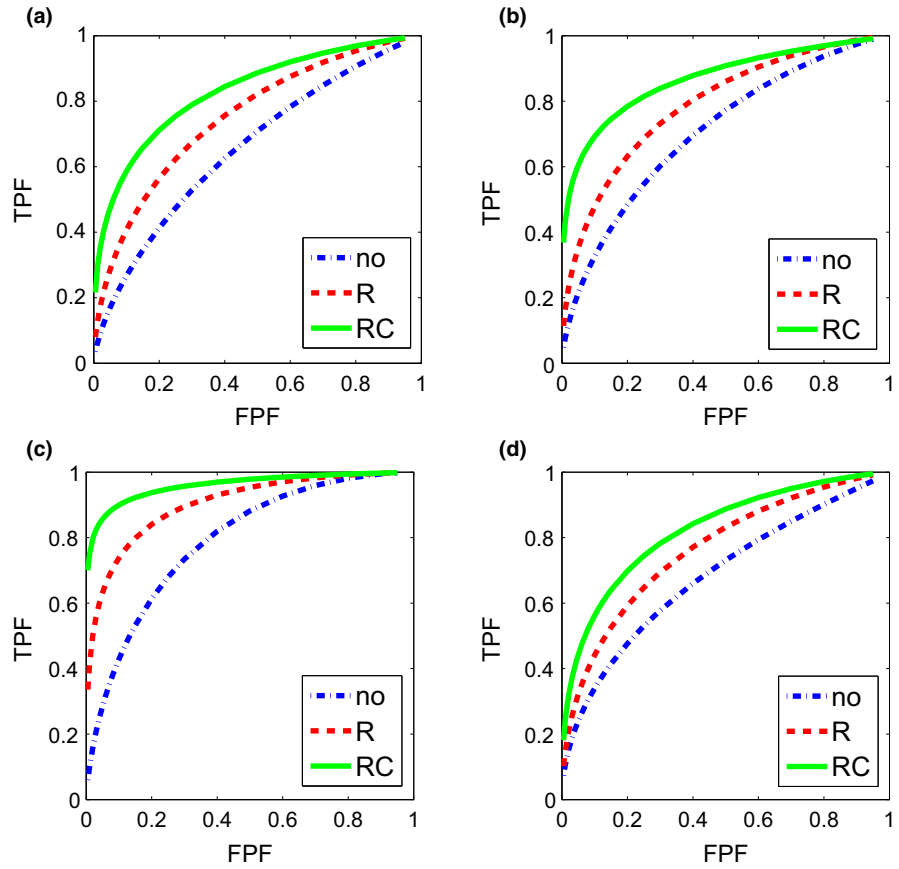

FIG. 6. ROC plots, true positive fraction (TPF) versus false positive fraction (FPF) for the task of distinguishing (a) the 50% nontransmural defect from the normal perfusion, (b) the 75% nontransmural defect from the normal perfusion, (c) the transmural defect from the normal perfusion, and (d) the 50% nontransmural from the transmural defect, from the standard XCAT phantom images reconstructed with the no motion correction (no), R motion-corrected (R), and RC motion-corrected (RC) methods. [Color figure can be viewed at wileyonlinelibrary.com]

respiratory and cardiac motion correction on the noise versus contrast recovery ratio is shown similarly in these customized XCAT phantoms. On a side note, when the same reconstruction method is applied, the contrast recovery ratio increases along the line of the 50% nontransmural, the 75% nontransmural, and the transmural defects for each of the three phantoms, which contributes to the same order of defect detectability shown below.

The task-based evaluation of the reconstruction methods for the standard XCAT phantom is shown in Fig. 6. Figure 6 presents the ROC curves from the standard XCAT phantom representing the detectability of (a) the 50% nontransmural defect from the normal perfusion, (b) the 75% nontransmural defect from the normal perfusion, (c) the transmural defect from the normal perfusion, and (d) the 50% nontransmural defect from the transmural defect. The AUC values (and standard deviations) of the ROC curves for the four tasks from the standard and the two customized XCAT phantom images with no motion correction (no), respiratory (R) motion correction, and respiratory and cardiac (RC) motion correction are presented in Fig. 7. In every task, the CLABROC tests between each of the two curves indicate that respiratory motion correction significantly improves the perfusion detection compared with no motion correction, and respiratory and cardiac motion correction significantly outperforms respiratory motion correction alone. The two-tailed *P*-values from all the comparisons, i.e., the respiratory motion correction compared with no motion correction as well as the respiratory and cardiac motion correction compared with the respiratory motion correction alone in each of the four tasks, are smaller than or equal to 0.02.

5. DISCUSSION

We performed mathematical and task-based analysis on the images reconstructed from the dual-gated MP PET data. As shown in the last section, the images demonstrated improved myocardium to blood pool contrast and improved noise versus normal to defect contrast tradeoff when the respiratory motion correction was applied and further so when the cardiac motion correction was then applied. Moreover, we showed statistically significant improvement in the detectability of both the two nontransmural (50% and 75%) and the transmural defects from normal perfusion and the improvement in separating the 50% nontransmural from the transmural defects, when applying the respiratory and cardiac motion correction. The mathematical evaluation results match the task-based evaluation results, i.e., that improvement in the

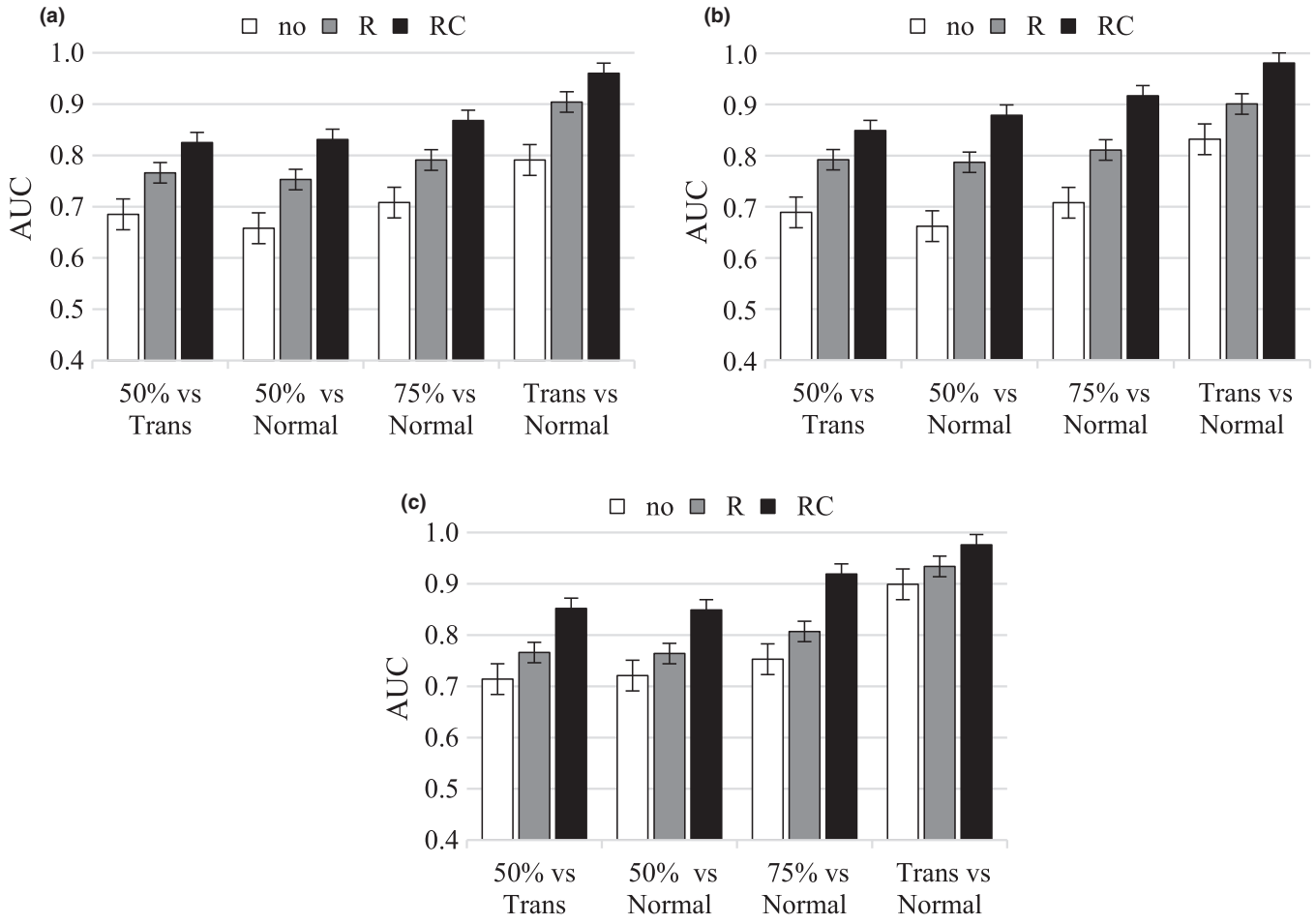

FIG. 7. AUC values of (a) the standard, (b) the volunteer A-customized, and (c) the volunteer B-customized XCAT phantoms for perfusion defect detection from the images reconstructed with no motion correction (no), R motion-corrected (R), and RC motion-corrected (RC) methods.

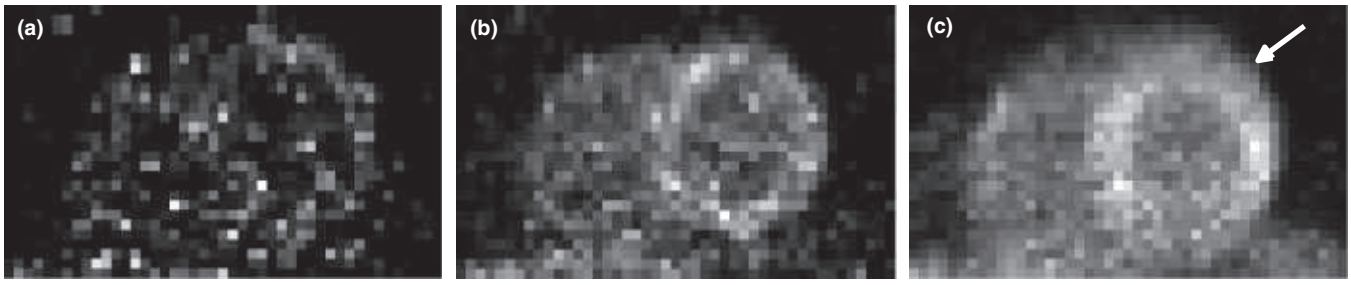

FIG. 8. Short-axis view of the images reconstructed with (a) R1C1 data, (b) R1Csum data, and (c) no gating data [repetition of figure 3(a1)] from the standard XCAT phantom. One noise realization of each case with a transmural defect, the arrow pointing to the defect.

mathematical criteria corresponds to improvement in the detectability of perfusion defects.

To show the effect of respiratory motion correction in cases with different motion amplitudes, we compared the respiratory motion correction results from the studies of the two volunteer phantoms. (Note that as of historical reasons, the version of the volunteer-specific phantoms is different from that of the standard XCAT phantom but the two customized phantoms are directly comparable.) The volunteer A has a larger respiratory motion amplitude ($\sim$2 cm) than that of the volunteer B ($\sim$0.7 cm).[46] As an example, the task of detecting the 50% nontransmural defect from the normal perfusion is used to illustrate the effect. Compared with no motion correction, the respiratory motion correction led to an increase in the contrast recovery ratio from 24% to 62% in the volunteer A and from 38% to 64% in the volunteer B. Moreover, the respiratory motion correction led to an improvement of the AUC value from 0.66 ± 0.03 to 0.79 ± 0.02 in the volunteer A and from 0.72 ± 0.03 to 0.76 ± 0.02 in the volunteer B. Therefore, we have demonstrated that the larger the respiratory motion amplitude, the more difference the respiratory motion correction makes in

measuring the normal to defect contrast and in detecting the MP defect. Furthermore, for motion amplitude as small as 0.7 cm carried by the volunteer B, respiratory motion correction still makes significant improvement in MP defect detection. On a side note, the effect of cardiac motion correction on the studies of the two volunteer phantoms are similar as they have comparable left ventricle volumes at the end-diastolic and end-systolic phases. The cardiac motion correction on top of the respiratory motion correction led to an improvement of the AUC value from 0.79 ± 0.02 to 0.88 ± 0.02 in the volunteer A and from 0.76 ± 0.02 to 0.85 ± 0.02 in the volunteer B.

In order to demonstrate the value of motion correction compared with gating only (no correction) methods, we conducted the ROC analysis on the dual-gated and the respiratory-gated data of the standard XCAT phantom. The respiratory and cardiac gate 1 data from dual gating (R1C1) and the respiratory gate 1 data from respiratory gating only (R1Csum) were used for image reconstruction. Figure 8 shows the short-axis view of the images reconstructed with the R1C1 data, the R1Csum data, and the no motion correction (no gating) data. The counts decrease in the R1Csum images compared with those in the images with no motion correction, and the counts further decrease in the R1C1 images. The task of detecting the 50% nontransmural defect from the normal perfusion was used as an example for comparison. The AUC value of using only the R and C gate 1 from the dual-gated data (R1C1) for reconstruction is 0.51 ± 0.02. It is significantly smaller than the AUC value of using the R gate 1 from only the R-gated data (R1Csum), which is 0.61 ± 0.02. These gated data reconstructed images lead to AUC values that are significantly smaller than those from no gating (0.66 ± 0.03) and hence smaller than those from gating with motion correction (0.75 ± 0.02 and 0.83 ± 0.02). Similar results were reached in the other three detection tasks.

As mentioned in the Introduction, Chan et al. demonstrated improved contrasts of normal myocardium to transmural or nontransmural defects in physical phantom images reconstructed from the end-expiration gate only data than those in images reconstructed from no gating data.[33] For validation purpose, we plotted contrast recovery vs noise curves for the reconstructed images from the R gate 1 data (R1Csum). Our results echo with those in the Chan et al. study[33] in the sense that we also see improvement in the contrasts (of R1Csum) compared with those from images with no motion correction (no gating). On the other hand, as expected, the noise increases in the R gate 1 images compared with that in the images with no motion correction. Therefore, the improvement in contrast led by taking one gate out of the gated data to 'freeze the motion' does not translate to improved detectability due to the accompanying noise rise caused by the considerably reduced count level. Motion correction among the gated data demonstrates its value leading to the improvement on defect detectability.

In Lamare et al. study mentioned in the Introduction, respiratory and cardiac motion compensated reconstruction (without separating the two movements) using nonrigid motion estimated from the dual-gated frames improved the myocardium to pool activity contrast compared with that with no motion correction.[35] To compare with their results, we also estimated the cardiac MVFs from the reconstructed respiratory motion-corrected cardiac gates (PET-MVFs) and applied them for cardiac motion correction. We compared the myocardium to pool contrast from the images using the PET-MVFs for cardiac motion correction (on top of respiratory motion correction) with that from the images without cardiac motion correction. Not surprisingly, we saw improved contrasts as shown in the Lamare et al. study.[35] However, the defect detection analysis on the respiratory and cardiac motion-corrected images using the PET-MVFs shows that the AUC values do not improve compared with those from no cardiac motion correction.

To investigate further, we plotted noise versus contrast recovery (normal to defect perfusion) curves for the respiratory and cardiac motion-corrected images with the PET-MVFs (not shown here). Compared with no cardiac motion correction, the contrast recovery improves. However, the noise significantly increases instead of reduces as shown in Fig. 5 in which the cardiac motion correction was performed with the MRI-MVFs. This experiment explicitly demonstrates the importance of using the MR images for cardiac motion estimation. It is also worth noting that the cardiac motion estimated from the T1-MR images does not represent the myocardial wall movement as its tangential component cannot be caught from the relatively uniform myocardium.[42] However, results from our perfusion defect detectability study demonstrate that the estimated MRI-MVFs serve the purpose of warping the cardiac gates to the reference gate similarly to the MVFs estimated from the tagged-MR images shown in the Petibon et al. study.[34]

Our next step is to perform physical phantom experiments before applying the proposed dual motion correction scheme to patient MP PET/MRI data. We plan to use a programmable respiratory motion platform (QUASAR Modus Medical Devices Inc., London, Ontario, Canada) to hold a Data Spectrum anthropomorphic torso phantom with a cardiac insert for the respiratory motion correction study. Scans will be performed to simulate a patient with transmural and nontransmural perfusion abnormalities. Before a respiratory motion simulation acquisition, a motion-free dataset will be acquired to serve as the ground truth. The effectiveness of respiratory motion correction will be assessed using the myocardium to pool contrast and the normal versus abnormal activity contrast.

It is worth mentioning that data-driven respiratory gating techniques have been developed for PET imaging, independent of hardware-based gating that measures the chest or abdominal wall excursion.[53,54] Data-driven gating techniques are not based on the assumption that external parameter measurement accurately reflects the respiratory state of the structure being imaged. We have also developed a data-driven respiratory gating technique to generate dual-gated sinograms

from processing list mode cardiac PET data with embedded ECG triggers. The proposed dual motion correction will be fully validated in patient study and move toward clinical cardiac PET/MRI applications.

6. CONCLUSION

We proposed a dual respiratory and cardiac motion correction scheme for MP PET data and studied its effectiveness on MP defect detection. The respiratory motion correction is incorporated within the 4D image reconstruction method, while the cardiac motion correction is performed afterward using the MVFs estimated from the corresponding cardiac-gated MR images. We evaluated our framework using both mathematical assessments and task-based analysis. The respiratory motion correction and cardiac motion correction were demonstrated to improve the myocardium to blood pool contrast and the trade-off between the noise and the normal to reduced perfusion contrast. Moreover, the detection of the transmural or the different levels of nontransmural defects from normal perfusion was significantly improved when the respiratory motion correction was applied and further enhanced after the cardiac motion correction. The classification of the transmural versus nontransmural defects was also improved by the developed motion correction framework. The proposed approach will have promising diagnostic and prognostic applications especially for integrated cardiac PET/MR imaging.

CONFLICT OF INTEREST

The authors have no relevant conflicts of interest to disclose.

ACKNOWLEDGMENTS

This work was supported in part by the NSF grants ECCS-1228091 and ECCS-1454552.

[a]Author to whom correspondence should be addressed. Electronic mail: jingtang@gmail.com.

REFERENCES

1. Hachamovitch R, Berman DS. The use of nuclear cardiology in clinical decision making. *Semin Nucl Med*. 2005;35:62–72.
2. Machac J. Cardiac positron emission tomography imaging. *Semin Nucl Med*. 2005;35:17–36.
3. Yoshinaga K, Chow BJW, Williams K, et al. What is the prognostic value of myocardial perfusion imaging using rubidium-82 positron emission tomography? *J Am Coll Cardiol*. 2006;48:1029–1039.
4. Bengel FM, Higuchi T, Javadi MS, Lautamäki R. Cardiac positron emission tomography. *J Am Coll Cardiol*. 2009;54:1–15.
5. Hachamovitch R, Hayes SW, Friedman JD, Cohen I, Berman DS. Comparison of the short-term survival benefit associated with revascularization compared with medical therapy in patients with no prior coronary artery disease undergoing stress myocardial perfusion single photon emission computed tomography. *Circulation*. 2003;107:2900–2907.
6. Tonino PA, De Bruyne B, Pijls NH, et al. Fractional flow reserve versus angiography for guiding percutaneous coronary intervention. *N Engl J Med*. 2009;360:213–224.
7. Thanavaro S, Krone RJ, Kleiger RE, et al. In-hospital prognosis of patients with first non-transmural and transmural infarctions. *Circulation*. 1980;61:29–33.
8. Zhang Y, Chan AK, Yu CM, et al. Strain rate imaging differentiates transmural from nontransmural myocardial infarction: a validation study using delayed-enhancement magnetic resonance imaging. *J Am Coll Cardiol*. 2005;46:864–871.
9. Rogers Jr WJ, Shapiro EP, Weiss JL, et al. Quantification of and correction for left ventricular systolic long-axis shortening by magnetic resonance tissue tagging and slice isolation. *Circulation*. 1991;84:721–731.
10. O'Dell WG, Moore CC, Hunter WC, Zerhouni EA, McVeigh ER. Three-dimensional myocardial deformations: calculation with displacement field fitting to tagged MR images. *Radiology*. 1995;195:829–835.
11. Slomka PJ, Nishina H, Berman DS, et al. Motion-frozen display and quantification of myocardial perfusion. *J Nucl Med*. 2004;45:1128–1134.
12. Wang Y, Vidan E, Bergman GW. Cardiac motion of coronary arteries: variability in the rest period and implications for coronary MR angiography. *Radiology*. 1999;213:751–758.
13. McLeish K, Hill DLG, Atkinson D, Blackall JM, Razavi R. A study of the motion and deformation of the heart due to respiration. *IEEE Trans Med Imag*. 2002;21:1142–1150.
14. Daou D. Respiratory motion handling is mandatory to accomplish the high-resolution PET destiny. *Eur J Nucl Med Mol Imaging*. 2008;35:1960–1970.
15. Livierato L, Rajappan K, Stegger L, Schafers K, Bailey DL, Camici PG. Respiratory gating of cardiac PET data in list-mode acquisition. *Eur J Nucl Med Mol Imaging*. 2006;33:584–588.
16. Dawood M, Büther F, Lang N, Schober O, Schäfers P. Respiratory gating in positron emission tomography: a quantitative comparison of different gating schemes. *Med Phys*. 2007;34:3067–3076.
17. Martinez-Möller A, Zikic D, Botnar R, et al. Dual cardiac-respiratory gated PET: implementation and results from a feasibility study. *Eur J Nucl Med Mol Imag*. 2007;34:1447–1454.
18. Büther F, Dawood M, Stegger L, et al. List mode-driven cardiac and respiratory gating in PET. *J Nucl Med*. 2009;50:674–681.
19. Teräs M, Kokki T, Durand-Schaefer, N, et al. Dual-gated cardiac PET-clinical feasibility study. *Eur J Nucl Med Mol Imag*. 2010;37:505–516.
20. Freiberg J, Hove JD, Kofoed KF, et al. Absolute quantitation of left ventricular wall and cavity parameters using ECG-gated PET. *J Nucl Cardiol*. 2004;11:38–46.
21. Castellani M, Colombo A, Giordano R. The role of PET with 13N-ammonia and 18F-FDG in the assessment of myocardial perfusion and metabolism in patients with recent AMI and intracoronary stem cell injection. *J Nucl Med*. 2010;51:1908–1916.
22. Nehmeh SA, Erdi YE. Respiratory motion in positron emission tomography/computed tomography: a review. *Semin Nucl Med*. 2008;38:167–176.
23. Rahmim A, Tang J, Zaidi H. Four-dimensional image reconstruction strategies in cardiac-gated and respiratory-gated PET imaging. *PET Clin*. 2013;8:51–67.
24. Klein J, Huesman H. Four-dimensional processing of deformable cardiac PET data. *Med Image Anal*. 2002;6:29–46.
25. Gigengack F, Ruthotto L, Burger M, Wolters CH, Jiang X, Schäfers KP. Motion correction in dual gated cardiac PET using mass-preserving image registration. *IEEE Trans Med Imaging*. 2012;31:698–712.
26. Li T, Thorndyke B, Schreibman E, Yang Y, Xing L. Model-based image reconstruction for four-dimensional PET. *Med Phys*. 2006;33:1288–1298.
27. Mair BA, Gilland R, Sun J. Estimation of images and nonrigid deformations in gated emission CT. *IEEE Trans Med Imaging*. 2006;25:1130–1144.
28. Qiao F, Pan T, Clark Jr JW, Mawlawi OR. A motion-incorporated reconstruction method for gated PET studies. *Phys Med Biol*. 2006;51:3769–3783.
29. Lamare F, Cresson T, Savean J, Cheze Le Rest C, Reader AJ, Visvikis D. Respiratory motion correction for PET oncology applications using

affine transformation of list mode data. *Phys Med Biol*. 2007;52:121–140.
30. Asma E, Manjeshwar R, Thielemans K. Theoretical comparison of motion correction techniques for PET image reconstruction. *IEEE Nucl Sci Symp Conf Rec*. 2006;3:1762–1767.
31. Chun SY, Fessler JA. Noise properties of motion-compensated tomographic image reconstruction methods. *IEEE Trans Med Imaging*. 2013;32:141–152.
32. Feng T, Wang J, Fung G, Tsui B. Non-rigid dual respiratory and cardiac motion correction methods after, during, before image reconstruction for 4D cardiac PET. *Phys Med Biol*. 2016;61:151–168.
33. Chan C, Harris M, Le M, et al. End-expiration respiratory gating for a high resolution stationary cardiac SPECT system. *Phys Med Biol*. 2014;59:6267–6287.
34. Petibon Y, Ouyang J, Zhu X, et al. Cardiac motion compensation and resolution modeling in simultaneous PET-MR: a cardiac lesion detection study. *Phys Med Biol*. 2013;58:2085–2102.
35. Lamare F, Le Maitre A, Dawood M, et al. Evaluation of respiratory and cardiac motion correction schemes in dual gated PET/CT cardiac imaging. *Med Phys*. 2014;41:072504.
36. Ratib O, Nkoulou R. Potential Applications of PET/MR Imaging in Cardiology. *J Nucl Med*. 2014;55:40S–46S.
37. Tsoumpas C, Mackewn JE, Halsted P, et al. Simultaneous PET-MR acquisition and MR-derived motion fields for correction of non-rigid motion in PET. *Ann Nucl Med*. 2010;24:745–750.
38. Shepp LA, Vardi Y. Maximum likelihood reconstruction for emission tomography. *IEEE Trans Med Imaging*. 1982;1:113–122.
39. Rahmim A, Tang J, Ay MR, Bengel FM. 4D respiratory motion-corrected Rb-82 myocardial perfusion PET imaging. *IEEE Nucl Sci Symp Conf Rec*. 2010;3312–3316.
40. Ng L, Ibanez L. Narrow band to image registration in the insight tookit. *Biomedical Image Registration*. 2003;2717:271–280.
41. Ibanez L, Schroeder W, Ng L, Cates J. *The ITK Software Guide: The Insight Segmentation and Registration Toolkit*. New York: Kitware Inc.; 2005.
42. Tang J, Segars WP, Lee TS, He X, Rahmim A, Tsui BMW. Quantitative study of cardiac motion estimation and abnormality classification in emission tomography. *Med Eng Phys*. 2011;33:563–572.
43. Love AEH. *A Treatise on the Mathematical Theory of Elasticity.* Cambridge: Cambridge University Press; 1994.
44. Veress AI, Segars WP, Tsui BMW, Weiss JA, Gullberg GT. Normal and pathological NCAT image and phantom data based on physiologically realistic left ventricle finite element models. *IEEE Trans Med Imaging*. 2006;25:1604–1616.
45. Segars WP, Sturgeon G, Mendonca S, Grimes J, Tsui BMW. 4D XCAT phantom for multimodality imaging research. *Med Phys*. 2010;37:4902–4915.
46. Könik A, Connolly CM, Johnson KL, et al. Digital anthropomorphic phantoms of nonrigid human respiratory and voluntary body motion for investigating motion correction in emission imaging. *Phys Med Biol*. 2014;59:3669–3682.
47. Tang J, Rahmim A, Lautamäki R, Lodge MA, Bengel FM, Tsui BMW. Optimization of Rb-82 PET acquisition and reconstruction protocols for myocardial perfusion defect detection. *Phys Med Biol*. 2009;54:3161–3171.
48. Benoit-Cattin H, Collewet G, Belaroussi B, Saint-Jaimes H, Odet C. The SIMRI project: a versatile and interactive MRI simulator. *J Magn Reson*. 2005;73:97–115.
49. Schulz V, Torres-Espallardo I, Renisch S, et al. Automatic, three-segment, MR-based attenuation correction for wholebody PET/MR data. *Eur J Nucl Med Mol Imaging*. 2011;38:138–152.
50. Wollenweber SD, Tsui BMW, Lalush DS, Frey EC, LaCroix KJ, Gullberg GT. Comparison of Hotelling observer models and human observers in defect detection from myocardial SPECT imaging. *IEEE Trans Nuc Sci*. 1999;46:2098–2103.
51. Metz CE, Shen JH, Herman BA. New methods for estimating a binormal ROC curve from continuously distributed test results. Annual Meeting of the American Statistical Association (Anaheim, CA), 1990.
52. Metz CE, Herman BA, Roe CA. Statistical comparison of two ROC-curve estimates obtained from partially-paired datasets. *Med Decis Making*. 1998;18:110–121.
53. Schleyer PJ, O'Doherty MJ, Barrington SF, Marsden PK. Retrospective data-driven respiratory gating for PET/CT. *Phys Med Biol*. 2009;54:1935–1950.
54. Wang M, Guo N, Zhang H, El Fhakri G, Hu G, Li Q. Retrospective data-driven respiratory gating for PET using TOF information. *Conf Proc IEEE Eng Med Biol Soc*. 2015;4520–4523.